

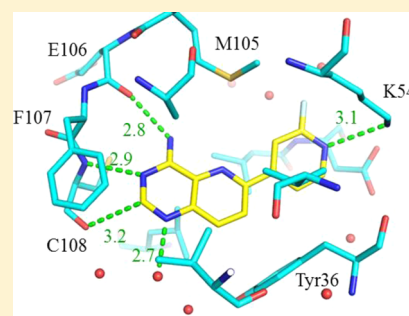
Discovery of Selective 4-Amino-pyridopyrimidine Inhibitors of MAP4K4 Using Fragment-Based Lead Identification and Optimization

Terry D. Crawford,* Chudi O. Ndubaku, Huifen Chen, Jason W. Boggs, Brandon J. Bravo, Kelly DeLaTorre, Anthony M. Giannetti, Stephen E. Gould, Seth F. Harris, Steven R. Magnuson, Erin McNamara, Lesley J. Murray, Jim Nonomiya, Amy Sambrone, Stephen Schmidt, Tanya Smyczek, Mark Stanley, Philip Vitorino, Lan Wang, Kristina West, Ping Wu, and Weilan Ye

Genentech Inc., 1 DNA Way, South San Francisco, California 94080, United States

S Supporting Information

ABSTRACT: Mitogen-activated protein kinase kinase kinase kinase 4 (MAP4K4) is a serine/threonine kinase implicated in the regulation of many biological processes. A fragment-based lead discovery approach was used to generate potent and selective MAP4K4 inhibitors. The fragment hit pursued in this article had excellent ligand efficiency (LE), an important attribute for subsequent successful optimization into drug-like lead compounds. The optimization efforts eventually led us to focus on the pyridopyrimidine series, from which 6-(2-fluoropyridin-4-yl)pyrido[3,2-*d*]pyrimidin-4-amine (**29**) was identified. This compound had low nanomolar potency, excellent kinase selectivity, and good in vivo exposure, and demonstrated in vivo pharmacodynamic effects in a human tumor xenograft model.

**INTRODUCTION**

Mitogen-activated protein kinase kinase kinase kinase 4 (MAP4K4, also known as HGK), a member of the sterile 20 (STE20) family of kinases,¹ is involved in a variety of signaling pathways. In particular, the expression and function of Map4k4 are linked to many physiological processes as well as pathological conditions, including metabolism,^{2–7} inflammation,⁸ neural degeneration,⁹ and cancer,^{10–15} suggesting that inhibiting MAP4K4 function may be beneficial in treating diseases associated with these processes. In order to further investigate MAP4K4 as a potential therapeutic target, identification of a potent and selective inhibitor will be necessary. However, there has been limited precedence for a selective small molecule MAP4K4 inhibitor in the literature.¹⁶ In the absence of suitable literature tool compounds, we conducted a screen of a diverse fragment library using surface plasmon resonance (SPR) with the aim of identifying a suitable hit for further development.¹⁷

RESULTS AND DISCUSSION

The fragment screen provided an array of hits with reasonable binding affinity ($K_d \approx 10–3400 \mu\text{M}$) and ligand efficiencies (225 hits with $\text{LE} > 0.35$).¹⁸ Several fragment hits were actively investigated, and this article will focus on the progression of the oxazole fragment (**1**, Figure 1A).¹⁹

On the basis of the chemical structure of **1** and comparisons with other known kinase inhibitors, we were confident that it was ATP-competitive and bound to the hinge region of the kinase utilizing the motif colored in red.²⁰ The docking model of **1** in the ATP-binding site of MAP4K4 (Figure 1B) was generated using the Glide program²¹ indicating that it formed a conventional as well as an atypical hydrogen bond to the hinge through the

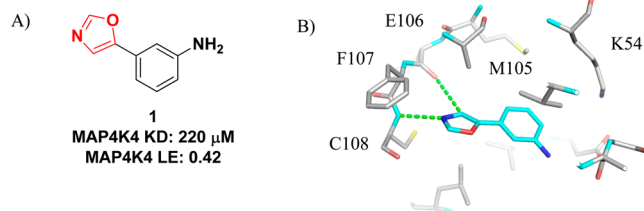


Figure 1. (A) Compound **1**. The red area of the molecule represents possible points of electrostatic contact with MAP4K4. (B) Predicted binding mode of compound **1** in the ATP binding site of MAP4K4 kinase domain crystal structure. Green dashed lines indicate potential intermolecular hydrogen bonds.

oxazole heterocycle while directing the aromatic group into a hydrophobic pocket adjacent to the methionine gatekeeper (Met105) and catalytic lysine (Lys54) (Figure 1B).²²

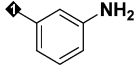
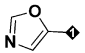
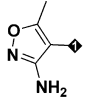
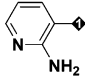
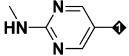
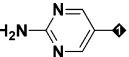
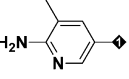
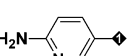
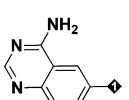
Our strategy for prosecuting this fragment was to pursue both close-in analogues of the oxazole as well as larger groups that would extend the fragment deeper into the hydrophobic pocket. In order to ensure that the optimization efforts did not deviate too far from ideal drug-like space, initial fragment follow-up compounds around **1** were restricted to a molecular weight less than 350 and cLogP less than 3.5.^{23,24} We hypothesized that replacing the oxazole with readily available hinge binding motifs with the ability to form two conventional hydrogen bonds could provide more efficient interactions and thereby enhance potency. As confirmation of this hypothesis, simple biaryl compounds

Received: January 28, 2014

Published: March 27, 2014

bearing complementary hydrogen bond donor/acceptor pairs (Table 1, 2–7) showed modest benefit in potency of up to 8-fold

Table 1. MAP4K4 SPR Binding Affinity of Oxazole Replacements with Hinge Binding Motifs

| Compound | Ar | MAP4K4 SPR K_d (μ M) | MAP4K4 SPR LE ^a | MAP4K4 SPR LLE ^a |
|----------|---|-----------------------------|----------------------------|-----------------------------|
| |  | | | |
| 1 |  | 220 | 0.42 | 2.56 |
| 2 |  | 351 | 0.34 | 2.46 |
| 3 |  | 65 | 0.41 | 2.49 |
| 4 |  | 28 | 0.42 | 3.05 |
| 5 |  | 175 | 0.37 | 3.08 |
| 6 |  | 68 | 0.38 | 2.20 |
| 7 |  | 510 | 0.32 | 1.70 |
| 8 |  | 4.3 | 0.41 | 2.40 |

^aSee Experimental Procedures for LE and LLE calculations.

improvement over the oxazole (1), while generally retaining high ligand efficiencies. Gratifyingly, extending the molecule with the quinazoline (8) showed a significant (55-fold) increase in potency, achieving a single digit micromolar dissociation constant as measured by SPR, while also maintaining ligand efficiency and lipophilic ligand efficiency levels comparable to those of 1.

Evaluation of compound 8 in a biochemical assay using a synthetic peptide substrate (Z'-LYTE)²⁵ demonstrated an IC₅₀ of 0.189 μ M (Table 2). With submicromolar biochemical potency achieved with our prototype compound 8, we advanced with biochemical activity as the primary assay from that point forward.

The structure–activity relationship (SAR) of the 6-aryl-1-aminoquinazoline scaffold was then explored further. Unsubstituted phenyl compound 9 (Table 2) was roughly 2-fold more potent than 8, suggesting some negative effects from inserting a meta-NH₂. Ortho-substitution on the phenyl group (e.g., 10) was not well tolerated presumably due to the large unfavorable torsional strain that results from binding into a nearly planar

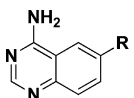
pocket within the protein as suggested by the docking model. Para substitutions also significantly decreased potency, indicating that the limit of the hydrophobic pocket had been reached (compounds 12, 15, 16, and 21). Halogens were well tolerated at the meta position, with the *m*-Cl (24) essentially equipotent and the *m*-F (19) being 2-fold more potent relative to the unsubstituted phenyl 9.

An X-ray cocrystal structure of compound 22 with the recombinant MAP4K4 kinase domain was solved (Figure 2). It revealed a “glove-like” fit for the ligand contained in the ATP-binding pocket and offered structure-based explanations for the SAR reported in Table 2. Importantly, the structure was consistent with the high ligand efficiency observed for the compound. The aminoquinazoline core forms two conventional hydrogen bonds and a weaker C–H type hydrogen bond with the kinase hinge residues Glu106 and Cys108. The substituted phenyl reaches into a hydrophobic pocket that is blocked off by a salt bridge between Lys54 and Asp171, which prevented further expansion at the para position while allowing small substitutions at either meta positions. Of particular note was the fact that the P-loop tyrosine side chain (Tyr36) swept down to form an edge to face interaction with the quinazoline core. Contemporaneous with this observation, a group at Pfizer published work suggesting that this folded P-loop conformation in MAP4K4 and a few other kinases may provide a potential opportunity for kinase selectivity.¹⁶ Since the halogen was involved in a favorable van der Waals interaction with the gatekeeper Met105, we also probed disubstituted aromatic substitutions off the 5 position, with 3-fluoro-5-aminophenyl 18 being equipotent to the 3-fluorophenyl.

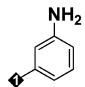
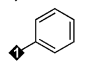
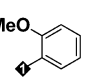
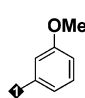
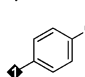
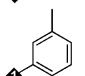
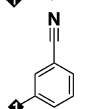
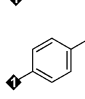
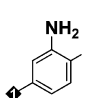
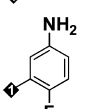
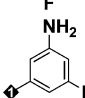
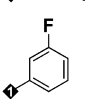
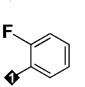
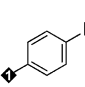
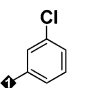
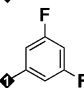
While this fragment progression showed a remarkable increase in potency through just two design iterations, the molecular properties were beginning to trend outside of the ideal drug-like space, particularly with respect to cLogP. This was of concern both with regard to instability in the *in vitro* liver microsome experiments, as well as the ability to achieve a desired PK profile *in vivo*. Evaluation of the ligand-lipophilicity efficiency (LLE)²⁶ of compounds in Table 2 validated this concern, as potency improvements from quinazoline 8 (LLE = 4.25) to 18, 19, and 22 did not improve their LLEs (4.48, 3.94, and 3.03, respectively). Further fragment optimization therefore focused on reducing lipophilicity through optimization of the core and also placing polar substituents on the periphery. To increase the polarity of the core, a nitrogen walk around the quinazoline core was undertaken (Table 3, 24–26).

Incorporation of nitrogen at the 7- or 8-positions (Table 3, 24 and 25) resulted in 100-fold and 35-fold losses in potency, respectively. This data highlights the importance of the P-loop Tyr36 edge to face interaction with the quinazoline core, which was weakened by the repulsive interactions between the lone pair of aromatic nitrogen and π -electrons of the Tyr36 side chain. Conversely, placement of a nitrogen at the 5-position (compound 26) resulted in a nearly 4-fold increase in potency, while maintaining an excellent LE (0.59) and also significantly improving the LLE relative to 19 (5.33 from 3.94). Possible reasons for the potency relative to lipophilicity improvement (Δ LLE = 1.40) could be that (1) the intramolecular hydrogen bond between the 4-amino and 5-aza would make the NH₂ group in 26 more planar, providing better conjugation of the amino group and also a better vector to the hinge, which will result in a stronger hydrogen bond between 4-amino and Glu106 backbone carbonyl and that (2) the addition of 5-aza in the core allows the

Table 2. MAP4K4 Affinities for 6-Aryl Derivatives of Quinazoline 8



The chemical structure shows a quinazoline ring system with an amino group (NH₂) at position 2 and an aryl group (Ar) at position 6.

| Compound | Ar | MAP4K4 IC ₅₀ (uM) ^a | MAP4K4 LE | MAP4K4 LLE | cLogP | HLM _h /MLM _h (ml/min/kg) ^b |
|----------|---|---|-----------|------------|-------|---|
| 8 |  | 0.189 | 0.51 | 4.25 | 2.4 | 14/80 |
| 9 |  | 0.121 | 0.56 | 3.89 | 3.2 | 20/85 |
| 10 |  | 0.546 | 0.45 | 3.02 | 3.1 | 17/82 |
| 11 |  | 0.33 | 0.47 | 2.93 | 3.3 | 19/82 |
| 12 |  | 0.689 | 0.43 | 2.64 | 3.3 | 19/80 |
| 13 |  | 0.423 | 0.49 | 2.68 | 3.7 | --/-- |
| 14 |  | 0.225 | 0.48 | 3.69 | 2.9 | --/-- |
| 15 |  | 1.70 | 0.42 | 2.69 | 2.9 | --/-- |
| 16 |  | 0.387 | 0.46 | 3.94 | 2.7 | --/-- |
| 17 |  | 0.351 | 0.47 | 4.26 | 2.5 | --/-- |
| 18 |  | 0.060 | 0.52 | 4.48 | 2.6 | 14/79 |
| 19 |  | 0.058 | 0.55 | 3.94 | 3.4 | --/-- |
| 20 |  | 0.297 | 0.50 | 3.17 | 3.3 | 19/86 |
| 21 |  | 0.381 | 0.49 | 2.89 | 3.4 | 18/85 |
| 22 |  | 0.077 | 0.54 | 3.03 | 4.0 | 19/81 |
| 23 |  | 0.132 | 0.50 | 3.12 | 3.6 | 17/64 |

^aIC₅₀ data are an average of at least 3 independent experiments. Each value has a standard deviation of less than one geometric mean (biochemical data with standard deviations can be found in the Supporting Information). ^bCompounds were incubated with mouse liver microsomes for 1 h, and the percent remaining was determined by LC-MS/MS analysis.

phenyl to adopt a smaller torsion angle (global minimum at 20 degrees) that is required for binding.

Pyridopyrimidine **26** had a cLogP value nearly a log unit lower than quinazoline **19** (cLogP = 2.6 vs 3.4), which returned the

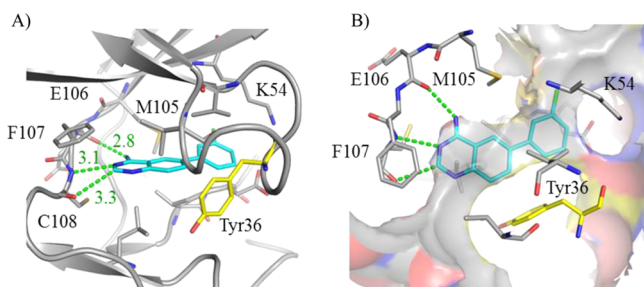


Figure 2. Crystal structure of **22** (cyan) in complex with MAP4K4. (PDB ID: 4OBO). (A) Binding details viewed from the opening of the ATP binding site with the hinge on the left and the N-terminal domain on top. The P-loop is folded down to enclose the compound with the side chain of Tyr36 (yellow sticks). Hydrogen bond interactions to the hinge are shown in green dashed lines, and distances are shown in Angstroms. (B) Binding details viewed from the top of the N-terminal domain. Solvent accessible surface of the binding site shows a snug fit of **22** in a hydrophobic channel formed by the kinase hinge, N- and C-terminal domains, and the folded-in P-loop.

Table 3. MAP4K4 Affinities for Pyridopyrimidine Positional Isomers Relating to **19** and **22**

| Compound | MAP4K4 IC ₅₀ (μM) ^a | MAP4K4 LE | MAP4K4 LLE | cLogP |
|---------------|--|--------------|---------------|-------|
| 19 | 0.058 | 0.55 | 3.94 | 3.4 |
| 24 | 5.84 | 0.40 | 2.08 | 3.2 |
| 25 | 2.12 | 0.43 | 3.22 | 2.5 |
| 26 | 0.017 | 0.59 | 5.33 | 2.6 |

^aIC₅₀ data are an average of at least 3 independent experiments. Each value has a standard deviation of less than one geometric mean (biochemical data with standard deviations can be found in the Supporting Information).

series back into the desired molecular property space and permitted further growth of the molecule to increase potency. Close-in analogues of **26** were then synthesized (Table 4, **27–34**) to explore the size of the hydrophobic pocket at the meta-position (**27**) as well as the potential favorable interactions with Asp171 (**28**) and the catalytic lysine (Lys54) (**29**).

The activities for **27–29** were essentially equipotent to **26**, with the additional H-bond interactions gained by **28** and **29** possibly offset by desolvation penalties. Notably, **29** demonstrated another significant improvement in LLE (6.34), indicating that we were driving this series into an excellent property space.

Analysis of the cocrystal structure of **29** in MAP4K4 indicated that the pyridine nitrogen does indeed form a hydrogen bond

with the Lys54 side chain (Figure 3). Compound **29** also showed a significantly improved stability profile compared to that of **26–28**, which established it as a viable lead molecule with the potential to have good in vivo stability.

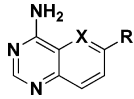
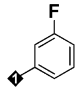
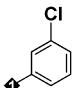
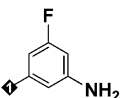
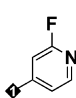
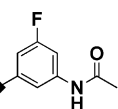
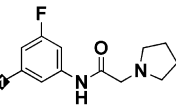
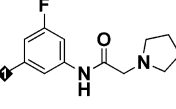
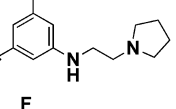
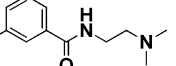
Acetamide **30** showed a significant decrease in potency relative to that of parent aniline **18**. This potency drop was expected based on the narrowness of the channel and the polar nature of the solvent exposed region as shown in Figure 2. Incorporation of a basic center into the amide tail with 2-pyrrolidinyl acetamide **31** resulted in potency equivalent to that of **18**. The crystal structure of **31** in complex with MAP4K4 showed that the basic center was critical for regaining potency lost from acetamide (**30**) due to its ability to disrupt the Lys54–Asp171 salt bridge (Figure 4). Lys54 was pushed out, while Asp171 formed a charge–charge interaction with the basic amine from the bound ligand. The carbonyl and amide nitrogen formed water-mediated hydrogen bonds to the protein. Incorporation of nitrogen at the 5 position of the quinazoline core (see Table 3 for numbering system) yielded amide **32** with 10 nM potency and moderate stability in human microsomes, although still poor in mouse microsomes. Attempts to reverse the amide (e.g., **34**) also resulted in a large drop in potency, while removing the carbonyl altogether to provide amine **33** resulted in a 15-fold potency decrease.

Kinase Selectivity. On the basis of the folded P-loop conformation that MAP4K4 adopts with the quinazoline and pyridopyrimidine-type ligands, we expected that they would exhibit significant selectivity over other kinases. An earlier lead, quinazoline **22** (Activity assay IC₅₀ = 77 nM), was screened in a kinase selectivity panel available from Invitrogen, and out of 61 kinases, only 2 showed >50% inhibition at 1 μM (Abl, Inh = 66%; Mink1, Inh = 84%) (Figure 5; the full selectivity table can be found in the Supporting Information). Notably, Abl is one of a few kinases capable of adopting the unusual folded P-loop conformation;¹⁶ therefore, activity of **22** against Abl was anticipated. Significant inhibition of kinase Mink1 was also expected, given that the ATP-binding pocket of Mink1 had ~100% sequence identity with that of MAP4K4 and the fact that they are closely related family members of MAP4K4. Compound **26** provided an 8-fold improvement in MAP4K4 potency while maintaining good kinase selectivity. Abl affinity was mitigated (11% at 1 μM), but modest PI4Kb activity was now observed (67% at 1 μM). Compound **32** showed the best selectivity profile over the 67 kinases screened, with only the inhibition of Mink1 showing activity >35% at 1 μM. Compound **29** showed modest TSSK1 (57% at 1 μM) and MARK1 (54% at 1 μM) affinity but was otherwise also highly selective considering that the 1 μM test concentration was ~60-fold higher than the MAP4K4 IC₅₀ (17 nM).

Pharmacokinetics/Pharmacodynamics. Because of their favorable in vitro profiles, the in vivo clearance of lead compounds **29** and **32** was assessed in female CD-1 mice (Table 5). Compound **32** showed a high clearance rate that was under-predicted by in vitro liver microsomes (Table 4). The rapid clearance was potentially due to amide cleavage by amidases or esterases. However, there was reasonable correlation between in vitro and in vivo clearance rates for **29**.

Oral exposure of **29** at a 5 mg/kg dose was a modest $F = 8.5\%$ (Table 5B). However, when a dose escalation study was conducted the AUC_{last} was nearly dose-proportional up to 150 mg/kg, and the free fraction exposure levels at this high dose suggested that **29** would have sufficient pathway engagement in vivo to elicit biomarker response. We have recently uncovered that inhibition of MAP4K4 by ATP-competitive small molecular

Table 4. MAP4K4 Affinities for Pyridopyrimidine Analogues Relating to 19 and 26

| Compound | X | R |  | | | | |
|----------|----|---|---|--------------|---------------|-------|--|
| | | | MAP4K4 IC ₅₀ (μM) ^a | MAP4K4 LE | MAP4K4 LLE | cLogP | HLM _h /MLM _h (ml/min/kg) ^b |
| 26 | N |  | 0.017 | 0.59 | 5.33 | 2.6 | 19/83 |
| 27 | N |  | 0.020 | 0.59 | 4.51 | 3.2 | 19/81 |
| 28 | N |  | 0.019 | 0.54 | 5.97 | 1.8 | 15/82 |
| 29 | N |  | 0.017 | 0.59 | 6.34 | 1.6 | 4.4/32 |
| 30 | CH |  | 1.60 | 0.36 | 3.48 | 2.7 | 7.3/68 |
| 31 | CH |  | 0.065 | 0.37 | 3.53 | 2.9 | 7.2/73 |
| 32 | N |  | 0.010 | 0.41 | 5.24 | 2.9 | 7.8/78 |
| 33 | N |  | 0.150 | 0.36 | 3.65 | 3.4 | 7/80 |
| 34 | N |  | 0.483 | 0.33 | 4.87 | 1.8 | 4/68 |

^aIC₅₀ data are an average of at least 3 independent experiments. Each value has a standard deviation of less than one geometric mean (biochemical data with standard deviations can be found in the Supporting Information). ^bCompounds were incubated with mouse liver microsomes for 1 h, and the percent remaining was determined by LC-MS/MS analysis.

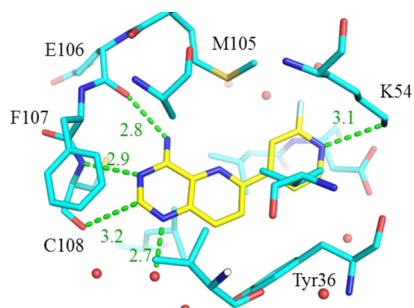


Figure 3. Crystal structure of compound 29 bound to the ATP binding site of MAP4K4 (PDB ID: 4OBP). Intermolecular hydrogen bonds are shown in green dashed lines, and distances are shown in Angstroms.

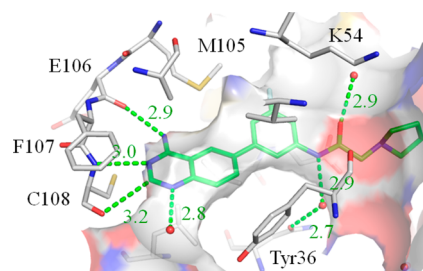


Figure 4. Crystal structure of compound 31 bound to the ATP binding site of MAP4K4 (PDB ID: 4OBQ). Intermolecular hydrogen bonds are shown in green dashed lines, and distances are shown in Angstroms.

inhibitor causes an elevation in phosphorylated (T181) MAP4K4 levels in vitro.²⁷ This finding indicated that ATP-

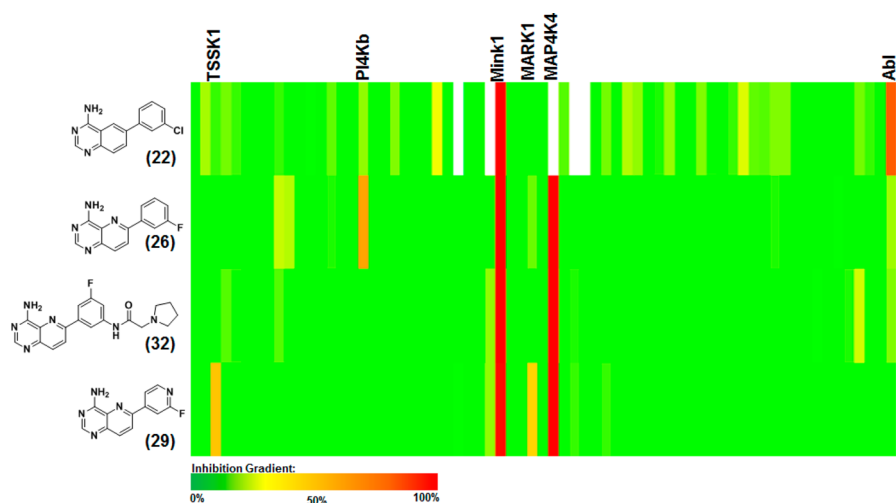


Figure 5. Heat map of Invitrogen kinase selectivity for **22**, **26**, **32**, and **29** at 1 μM . Bands are colored according to a progressive color gradient, with green indicating 0% inhibition and red as 100% inhibition (white indicates no data available for that kinase). The complete table of kinase inhibition data can be found in the Supporting Information.

Table 5. Summary of PK Parameters Following IV Bolus (A) and PO (B) Administration in Female CD-1 Mice

| (A) | | | | | |
|-----------|--------------|---|------------------------------------|----------------------|------------------------|
| analyte | dose (mg/kg) | AUC _{0-∞} (h· μM) | CL (mL/min/kg) | T _{1/2} (h) | V _{ss} (L/kg) |
| 32 | 1 | 0.25 ± 0.01 | 174.0 ± 3.8 | 0.34 ± 0.23 | 3.9 ± 1.7 |
| 29 | 1 | 5.99 ± 0.62 | 11.6 ± 1.3 | 0.56 ± 0.05 | 0.6 ± 0.03 |
| (B) | | | | | |
| analyte | dose (mg/kg) | AUC _{last} (h· μM) | C _{max} (μM) | T _{max} (h) | F (%) |
| 32 | 5 | 0.35 ± 0.04 | 0.15 ± 0.04 | 0.33 ± 0.14 | 5.7 ± 0.5 |
| 29 | 5 | 2.55 ± 0.21 | 1.33 ± 0.28 | 1.00 ± 0.00 | 8.5 ± 0.7 |
| 29 | 50 | 30.3 ± 9.12 | 6.34 ± 0.84 | 0.83 ± 0.29 | 23.6 ± 7.1 |
| 29 | 100 | 41.2 ± 26.2 | 7.65 ± 4.62 | 2.67 ± 2.89 | 16.0 ± 10.2 |
| 29 | 150 | 107.0 ± 22.5 | 14.5 ± 3.1 | 6.0 ± 3.0 | 27.8 ± 5.8 |

competitive MAP4K4 inhibitor-induced elevation of MAP4K4-pT181 constitutes a pharmacodynamic (PD) response. Therefore, treatment of mice with a potent and selective MAP4K4 inhibitor such as **29** would be expected to elicit similar PD response in vivo provided there is sufficient exposure. Compound **29** was evaluated for its ability to induce a PD response in HT-1080 human fibrosarcoma xenograft tumors. After a single oral dose of compound **29**, plasma and tumor samples were isolated at 4 and 24 h time points. PD response was assessed through Western blotting of MAP4K4-pT181 normalized to total MAP4K4. Compound **29** caused a dose-dependent increase in pMAP4K4 (T181) at both time points above the baseline of the vehicle-treated mice (Figure 6).

Chemistry. Fragment analogues (**2–8**) were synthesized by Suzuki coupling of commercially available 3-aminophenylboronic acid with appropriate aryl bromides. Fragments derived from 6-aryl quinazoline (**9–23**) were prepared in a similar fashion with commercial 4-amino-6-bromoquinazoline and phenylboronic acids (Scheme 1).

Pyridopyrimidine analogues **24–27** were synthesized as described in Scheme 2. Cyclization of 3-amino-6-chloropicolinamide (**37**) with triethylorthoformate yielded pyridopyrimidinone **38**.²⁸ Chlorination with refluxing thionyl chloride afforded chloropyrimidine **39**, followed by amination with ammonia to give amine **40**. Subsequent Suzuki coupling reactions then provided analogue **26**. The regioisomeric pyridopyrimidinone intermediate **42** was derived by cyclization of amino acid **41** with

formamide.²⁹ Analogue **27** was synthesized via the same route as **26**.

CONCLUSIONS

Herein we described the discovery of a potent, ligand efficient, and highly selective series for inhibition of MAP4K4. By taking a different approach than most conventional FBDD efforts, we incorporated a broad scope of structural diversity relative to the initial hit to quickly obtain compounds that possessed nanomolar biochemical activity. Subsequently, we focused on fine-tuning the scaffold to optimize the lipophilic ligand efficiency of the compounds. The series benefitted by the folded P-loop conformation, which helped to impart high ligand efficiency and superb kinase selectivity. These efforts culminated in the identification of compound **29**, a low molecular weight MAP4K4 inhibitor that had favorable in vivo PK properties. Compound **29** was evaluated in a PD experiment where it demonstrated pathway functional response. The discovery of this compound paved the way for further lead optimization efforts, which will be the subject of future communications.

EXPERIMENTAL PROCEDURES

General Methods. All solvents and reagents were used as obtained. Reactions involving air or moisture sensitive reagents were carried out under nitrogen atmosphere. Microwave reactions were performed using CEM Discover and Biotage Initiator reactors. NMR spectra were recorded in a deuterated solvent with Varian Avance 300-MHz or Bruker Avance 400- or 500-MHz NMR spectrometers and referenced to

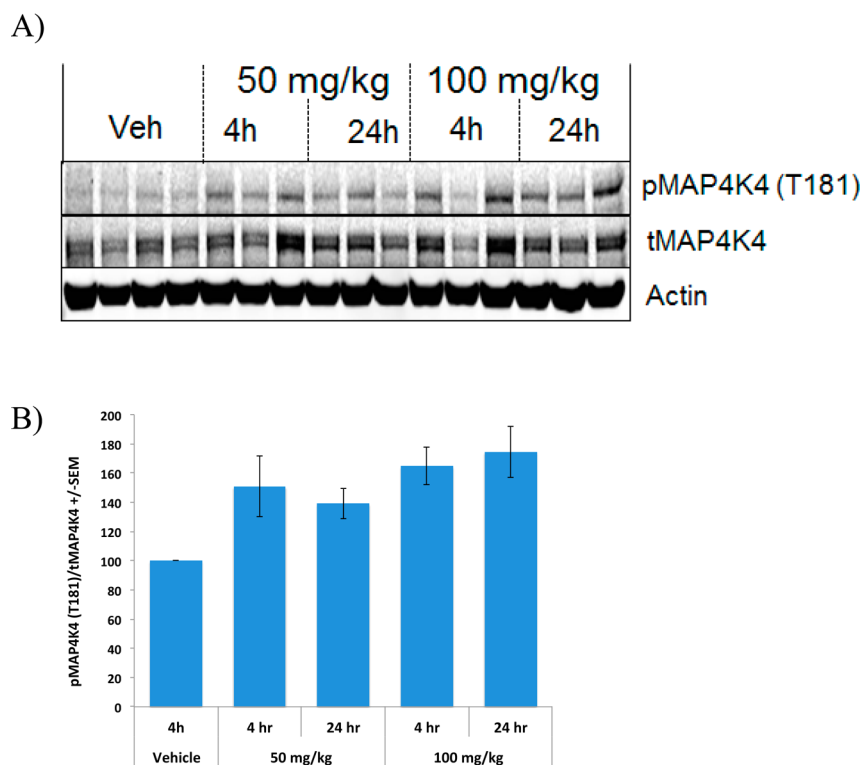
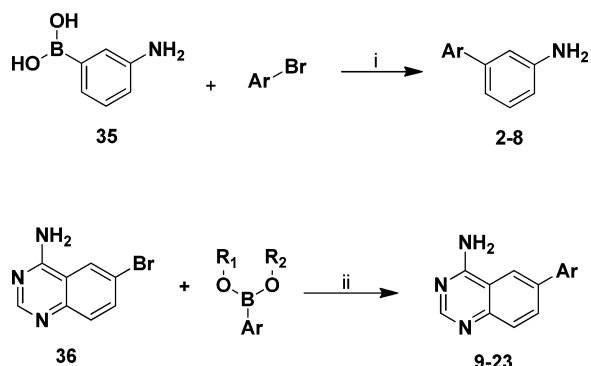


Figure 6. (A) Pharmacodynamic evaluation of compound **29** in HT-1080 human fibrosarcoma xenografts. (B) Quantitation of the p-MAP4K4 levels normalized by total MAP4K4 over a 24 h period. Error bars correspond to the standard error of the means.

Scheme 1. Suzuki Couplings to Afford Compounds **2–23**^a



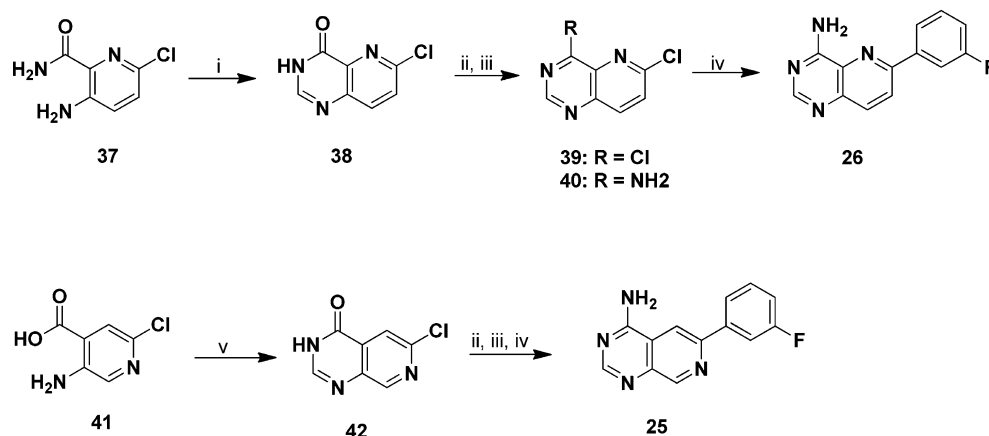
^aReagents and conditions: (i) bis(*di-tert*-butyl(4-dimethylaminophenyl)phosphine)dichloropalladium(II), potassium acetate, acetonitrile/water, 80 °C; (ii) bis(*di-tert*-butyl(4-dimethylaminophenyl)phosphine)dichloropalladium(II), potassium phosphate tribasic, dioxane/water, 100 °C.

trimethylsilane (TMS). Chemical shifts are expressed as δ units using TMS as the external standard (in NMR descriptions, s = singlet, d = doublet, t = triplet, q = quartet, m = multiplet, and br = broad peak). All coupling constants (J) are reported in Hertz. Mass spectra were measured with a Finnigan SSQ710C spectrometer using an ESI source coupled to a Waters 600MS HPLC system operating in reverse mode with an X-bridge Phenyl column of dimensions 150 mm \times 2.6 mm, with 5 μ m-sized particles. Preparatory-scale silica gel chromatography was performed using medium-pressure liquid chromatography (MPLC) on a CombiFlash Companion (Teledyne ISCO) with RediSep normal phase silica gel (35–60 μ m) columns and UV detection at 254 nm. Reverse-phase high performance liquid chromatography (HPLC) was used to purify compounds where indicated by elution on a Waters 3100 mass-directed prep instrument using a Phenomenex Gemini-NX C18 column (20.2 \times 50 mm, 5 μ m) as stationary phase using the mobile

phase indicated and operating at a 35 mL/min flow rate. Chemical purities were >95% for all final compounds as assessed by LCMS analysis. The following analytical method was used to determine chemical purity of final compounds: HPLC-Agilent 1200, water with 0.05% TFA, acetonitrile with 0.05% TFA, Agilent SB-C18, 1.8 μ M, 2.1 \times 30 mm, 25 °C, 3–95% B in 8.5 min, 95% in 2.5 min, 400 μ L/min, 220 and 254 nm, equipped with Agilent quadrupole 6140, ESI positive, and 90–1300 amu.

MAP4K4 SPR-Based Fragment Screen. MAP4K4 (residues 3–328) containing an N-terminal His-tag and a C-terminal Avi-tag (Avidity, LLC) was biotinylated during baculovirus expression and purified to homogeneity by nickel-affinity and size-exclusion chromatography. Mass analysis indicated that there was no phosphorylation of the purified material. For SPR experiments, the biotinylated protein was captured to CM5 chips (GE Healthcare) manually coupled with \sim 8,000 RUs of neutravidin (Pierce) inside a Biacore T100 (GE Healthcare) as previously described.³⁰ After priming into the experimental running buffer (50 mM HEPES, pH 7.2, 150 mM NaCl, 2 mM MgCl₂, 1 mM TCEP, 0.01% Tween-20, 1% PEG-3350, and 5% DMSO), 4,000–8,000 RUs of M4K4 was generally captured. Good long-term binding stability of the surface was observed during pilot fragment screening that included the use of a control compound with a K_D of 1 μ M and a dissociation half-life of \sim 3 s. A screen of the Genentech edition one fragment library (\sim 2,500 compounds) was executed using a single-point screen at 100 μ M compound. Raw sensorgram data were reduced, solvent corrected, double reference inspected for poor sensorgrams and aggregating compounds,³¹ and fit using Scrubber II (BioLogic Software, Campbell, Australia; <http://www.biologic.com.au>). Primary data were additionally corrected for drift, daily solvent mismatches, and scaled to fractional binding occupancy using BioBook (IDBS) as previously discussed.³⁰ Approximately 300 hits were further characterized in a dose–response format by SPR at 200 μ M in a 2-fold dilution series to yield K_D and LE information. A total of 225 hits were characterized and confirmed with a K_D range of 10 to 2000 μ M and LEs ranging from 0.24 to 0.59 with a median of 0.33.

MAP4K4 Inhibition Biochemical Assay Protocol. The kinase activity of purified human MAP4K4 kinase domain on a peptide

Scheme 2. Preparation of Pyridopyrimidine^a

^aReagents and conditions: (i) (EtO)₃CH, reflux, 3 h; (ii) thionyl chloride, cat. DMF, 85 °C, 3 h; (iii) 7 N NH₃/MeOH, 50 °C, 2 h; (iv) bis(*di-tert*-butyl(4-dimethylaminophenyl)phosphine) dichloropalladium(II), potassium phosphate tribasic, dioxane/water, 100 °C; (v) formamide, 130 °C, 12 h.

substrate (5-FAM-LGRDKYKTLRQIRQ-COOH) was monitored using Z'-LYTE technology according to the manufacturer's protocol.

Ligand Efficiency (LE) and Ligand-Lipophilicity Efficiency (LLE) calculations. SPR LE and LLE calculated as $LE = -RT \ln(K_d) / N_{\text{heavy atoms}}$. LLE = $pK_d - c\text{LogP}$. Biochemical assay LE = $-RT \ln(IC_{50}) / N_{\text{heavy atoms}}$. LLE = $pIC_{50} - c\text{LogP}$.

6-Chloropyrido[3,2-*d*]pyrimidin-4(3H)-one (38). To a round-bottomed flask was added 3-amino-6-chloro-pyridine-2-carboxamide **32**, (9.0 g, 52.5 mmol) and 100 mL of triethoxymethane. The reaction was stirred at reflux for 3 h. The reaction was then cooled to room temperature and the white solid collected by filtration. The precipitate was then purified by flash column chromatography (3–10% MeOH/DCM) yielding 4.6 g of product as a white solid (48%). ¹H NMR (400 MHz, DMSO) δ 12.69 (s, 1H), 8.19 (s, 1H), 8.14 (d, *J* = 8.6 Hz, 1H), 7.88 (d, *J* = 8.6 Hz, 1H).

4,6-Dichloropyrido[3,2-*d*]pyrimidine (39). To a round-bottomed flask was added 6-chloro-3H-pyrido[3,2-*d*]pyrimidin-4-one (4.6 g, 25.33 mmol), followed by thionyl chloride (80 mL) and DMF (0.05 mL). The reaction was stirred at 85 °C for 3 h, at which point the reaction was a clear solution. The reaction was then concentrated via rotovap and azeotroped 3× with chloroform. The crude product was dried overnight on high vacuum and then carried forward to the amination step without purification.

6-Chloropyrido[3,2-*d*]pyrimidin-4-amine (40). To 4,6-dichloropyrido[3,2-*d*]pyrimidine (5.0 g, 25 mmol) was added 30 mL of 7 M ammonia in methanol (210 mmol), and then it was stirred at 50 °C for 2 h. The reaction was then concentrated via rotovap and triturated with dichloromethane. The filter cake was then washed with water 3× to yield a clean product; 2.83 g as a yellow solid (62% over two steps). ¹H NMR (400 MHz, DMSO) δ 8.44 (s, 1H), 8.13 (d, *J* = 8.8 Hz, 1H), 8.02 (bs, *J* = 14.8 Hz, 1H), 7.89 (bs, 1H), 7.86 (d, *J* = 8.8 Hz, 1H).

6-(3-Fluorophenyl)pyrido[3,2-*d*]pyrimidin-4-amine (26). To an 8 mL screw-cap vial was added 6-chloropyrido[3,2-*d*]pyrimidin-4-amine (75 mg, 0.42 mmol), (3-fluorophenyl)boronic acid (87 mg 0.62 mmol), bis(*di-tert*-butyl(4-dimethylaminophenyl)phosphine) dichloropalladium(II) (15 mg, 0.021 mmol), potassium phosphate tribasic (0.63 mL, 2.00 mol/L in water 1.25 mmol), and 1,4-dioxane (0.75 mL). The mixture was capped and shaken at 100 °C for 2 h. The reaction was cooled to room temperature, diluted with 4 mL of DCM, and washed with 2 mL of water. Combined organics were concentrated under reduced pressure. The residue was purified by prep HPLC (5% to 85% acetonitrile with 0.1% ammonium hydroxide in 8 min gradients) yielded of 6-(3-fluorophenyl)pyrido[3,2-*d*]pyrimidin-4-amine (51 mg, 51%). ¹H NMR (400 MHz, DMSO) δ 8.48 (d, *J* = 8.9 Hz, 1H), 8.44–8.38 (m, 2H), 8.30–8.18 (m, 2H), 8.15 (d, *J* = 8.8 Hz, 1H), 7.99 (bs, 1H), 7.62–7.53 (m, 1H), 7.36–7.29 (m, 1H). LCMS *m/z* (M + H) 241.

6-(2-Fluoropyridin-4-yl)pyrido[3,2-*d*]pyrimidin-4-amine (29). To 6-chloropyrido[3,2-*d*]pyrimidin-4-amine (4.0 g, 22.2 mmol) in 100 mL of acetonitrile was added 2-fluoro-4-(4,4,5,5-tetramethyl-1,3,2-dioxaborolan-2-yl)pyridine (5.93 g, 26.6 mmol), [1,1'-bis-(diphenylphosphino)ferrocene]dichloropalladium(II), complex with dichloromethane (1.62 g, 2.2 mmol), and 66 mL of 1 M potassium carbonate in water (66 mmol). The reaction was heated to 80 °C for 1 h. The crude was filtered through a thin layer of Celite, and the solid was then treated with 250 mL of ethanol and heated to reflux. The solid was filtered, then triturated with ethyl acetate and methanol to afford 6-(2-fluoropyridin-4-yl)pyrido[3,2-*d*]pyrimidin-4-amine (5.3 g, 99%). ¹H NMR (400 MHz, DMSO) δ 8.61 (d, *J* = 8.8 Hz, 1H), 8.46 (s, 2H), 8.42 (d, *J* = 5.3 Hz, 1H), 8.37 (d, *J* = 5.3 Hz, 1H), 8.34 (s, 1H), 8.22 (d, *J* = 8.8 Hz, 1H), 8.12 (s, 1H). LCMS *m/z* (M + H) 242.

Modeling Methods. The molecular modeling software available through the Maestro interface (Schrodinger, Inc.)²¹ were used for ligand preparation and docking. Starting ligand conformations for all compounds were prepared by LigPrep at pH 7.0 ± 1 using default parameters. The prepared ligand structures were then docked into the ATP-binding site of a MAP4K4 crystal structure (2.35 Å) in complex with an HTS hit (not published) using Glide SP. The docking poses were evaluated based on a combination of criteria including the Glide docking score, the formation of hydrogen bond(s) to the hinge residues Glu106 and Cys108, other favorable intermolecular interactions, low strain energy of the bound ligand ($E_{\text{strain}} < 2$ kcal/mol), etc. All of the docking model and X-ray structure figures were produced using the software PyMOL (Schrodinger, Inc.).²¹

■ ASSOCIATED CONTENT

📄 Supporting Information

PK study protocols and analysis; PD in vitro and in vivo analysis; single point inhibition Invitrogen kinase selectivity data for **22**, **26**, **32**, and **29**; protein purification and crystallization; preparation and characterization of **2–25**, **27–28**, and **30–34**; and biochemical assay data with standard deviations. This material is available free of charge via the Internet at <http://pubs.acs.org>.

Accession Codes

PDB accession codes: 4OBO, 4OBP, and 4OBQ.

■ AUTHOR INFORMATION

Corresponding Author

*E-mail: terrydc@gene.com. Phone: 650-467-8895.

Notes

The authors declare no competing financial interest.

ACKNOWLEDGMENTS

We thank Mengling Wong, Chris Hamman, Michael Hayes, and Shi Choong for compound purification. Baiwei Lin, Deven Wang, and Yutao Jiang are acknowledged for analytical support. Grady Howes' and Gigi Yuen's help with compound management and logistics is also recognized, as is the help from Jinhua Chen and Charles Ding (Wuxi Apptec) with technical support. Finally, Chris Lewis, Bing-Yan Zhu, Jeff Blaney, and Sarah Hymowitz are thanked for project support.

ABBREVIATIONS USED

cLogP, calculated LogP; DCM, dichloromethane; DMF, dimethylformamide; DMSO- d_6 , deuterated DMSO; EGTA, ethylene glycol-bis(2-aminoethyl ether)- N,N,N',N' -tetraacetic acid; (EtO) $_3$ CH, triethylorthoformate; FA, formic acid; HATU, 2-(7-aza-1H-benzotriazole-1-yl)-1,1,3,3-tetramethyluronium hexafluorophosphate; HEPES, 2-[4-(2-hydroxyethyl)-piperazin-1-yl]ethanesulfonic acid; Log $D_{7.2}$, log of partition coefficient between octanol and pH $_{7.2}$ aqueous buffer; MCT, methyl cellulose/tween; MeOH, methanol; PMSF, phenylmethylsulfonyl fluoride; SPR, surface plasmon resonance; TBST, tris buffered saline with Tween 20; TCEP, 3,3',3''-phosphanetriyltripropanoic acid; TEA, triethylamine

REFERENCES

(1) Dan, I.; Watanabe, N. M.; Kusumi, A. The Ste20 group kinases as regulators of MAP kinase cascades. *Trends Cell Biol.* **2001**, *11*, 220–230.

(2) Tang, X. An RNA interference-based screen identifies MAP4K4/NIK as a negative regulator of PPAR, adipogenesis, and insulin-responsive hexose transport. *Proc. Natl. Acad. Sci. U.S.A.* **2006**, *103*, 2087–2092.

(3) Baumgartner, M.; Sillman, A. L.; Blackwood, E. M.; Srivastava, J.; Madson, N.; Schilling, J. W.; Wright, J. H.; Barber, D. L. The Nck-interacting kinase phosphorylates ERM proteins for formation of lamellipodium by growth factors. *Proc. Natl. Acad. Sci. U.S.A.* **2006**, *103*, 13391–13396.

(4) Bouzakri, K.; Zierath, J. R. MAP4K4 gene silencing in human skeletal muscle prevents tumor necrosis factor- α -induced insulin resistance. *J. Biol. Chem.* **2007**, *282*, 7783–7789.

(5) Bouzakri, K.; Ribaux, P.; Halban, P. A. Silencing mitogen-activated protein kinase 4 (MAP4K4) protects beta cells from tumor necrosis factor- α -induced decrease of IRS-2 and inhibition of glucose-stimulated insulin secretion. *J. Biol. Chem.* **2009**, *284*, 27892–27898.

(6) Tesz, G. J.; Guilherme, A.; Guntur, K. V. P.; Hubbard, A. C.; Tang, X.; Chawla, A.; Czech, M. P. Tumor necrosis factor α (TNF α) stimulates Map4k4 expression through TNF α receptor 1 signaling to c-Jun and activating transcription factor 2. *J. Biol. Chem.* **2007**, *282*, 19302–19312.

(7) Zhao, X.; Mohan, R.; Özcan, S.; Tang, X. MicroRNA-30d induces insulin transcription factor MafA and insulin production by targeting mitogen-activated protein kinase 4 (MAP4K4) in pancreatic β -cells. *J. Biol. Chem.* **2012**, *287*, 31155–31164.

(8) Aouadi, M.; Tesz, G. J.; Nicoloso, S. M.; Wang, M.; Chouinard, M.; Soto, E.; Ostroff, G. R.; Czech, M. P. Orally delivered siRNA targeting macrophage Map4k4 suppresses systemic inflammation. *Nature* **2009**, *458*, 1180–1184.

(9) Loh, S. H. Y.; Francescut, L.; Lingor, P.; Bähr, M.; Nicotera, P. Identification of new kinase clusters required for neurite outgrowth and retraction by a loss-of-function RNA interference screen. *Cell Death Differ.* **2007**, *15*, 283–298.

(10) Wright, J. H.; Wang, X.; Manning, G.; LaMere, B. J.; Le, P.; Zhu, S.; Khatry, D.; Flanagan, P. M.; Buckley, S. D.; Whyte, D. B.; Howlett, A. R.; Bischoff, J. R.; Lipson, K. E.; Jallal, B. The STE20 kinase HGK is

broadly expressed in human tumor cells and can modulate cellular transformation, invasion, and adhesion. *Mol. Cell. Biol.* **2003**, *23*, 2068–2082.

(11) Collins, C. S.; Hong, J.; Sapinoso, L.; Zhou, Y.; Liu, Z.; Micklash, K.; Schultz, P. G.; Hampton, G. M. A small interfering RNA screen for modulators of tumor cell motility identifies MAP4K4 as a promigratory kinase. *Proc. Natl. Acad. Sci. U.S.A.* **2006**, *103*, 3775–3780.

(12) Liu, A. W.; Cai, J.; Zhao, X. L.; Jiang, T. H.; He, T. F.; Fu, H. Q.; Zhu, M. H.; Zhang, S. H. ShRNA-targeted MAP4K4 inhibits hepatocellular carcinoma growth. *Clin. Cancer Res.* **2011**, *17*, 710–720.

(13) Liang, J. J.; Wang, H.; Rashid, A.; Tan, T.-H.; Hwang, R. F.; Hamilton, S. R.; Abbruzzese, J. L.; Evans, D. B.; Wang, H. Expression of MAP4K4 is associated with worse prognosis in patients with stage II pancreatic ductal adenocarcinoma. *Clin. Cancer Res.* **2008**, *14*, 7043–7049.

(14) Qiu, M.-H.; Qian, Y.-M.; Zhao, X.-L.; Wang, S.-M.; Feng, X.-J.; Chen, X.-F.; Zhang, S.-H. Expression and prognostic significance of MAP4K4 in lung adenocarcinoma. *Pathol. Res. Pract.* **2012**, *208*, 541–548.

(15) Mao, J.; Ligon, K. L.; Rakhlin, E. Y.; Thayer, S. P.; Bronson, R. T.; Rowitch, D.; McMahon, A. P. A novel somatic mouse model to survey tumorigenic potential applied to the hedgehog pathway. *Cancer Res.* **2006**, *66*, 10171–10178.

(16) Guimarães, C. R. W.; Rai, B. K.; Munchhof, M. J.; Liu, S.; Wang, J.; Bhattacharya, S. K.; Buckbinder, L. Understanding the impact of the P-loop conformation on kinase selectivity. *J. Chem. Inf. Model.* **2011**, *51*, 1199–1204.

(17) Erlanson, D. A. Introduction to Fragment-Based Drug Discovery. In *Fragment-Based Drug Discovery and X-Ray Crystallography*; Topics in Current Chemistry; Springer: Berlin, Germany, 2011; Vol. 317, pp 1–32.

(18) Abad-Zapatero, C. Ligand efficiency indices for effective drug discovery. *Expert Opin. Drug Discovery* **2007**, *2*, 469–488.

(19) A full description of other fragment expansion campaigns will be described in short order. Wang, L., et al., manuscript in Preparation.

(20) Traxler, P.; Furet, P. Strategies toward the design of novel and selective protein tyrosine kinase inhibitors. *Pharmacol. Ther.* **1999**, *82*, 195–206.

(21) *Maestro/Glide/PyMOL*; Schrödinger, Inc.: New York.

(22) At this stage in the hit triage, X-ray crystal structures of fragments in complex with MAP4K4 were of too low a resolution to be interpretable.

(23) Mauser, H.; Stahl, M. Chemical fragment spaces for de novo design. *J. Chem. Inf. Model.* **2007**, *47*, 318–324.

(24) Lipinski, C. A.; Lombardo, F.; Dominy, B. W. Experimental and computational approaches to estimate solubility and permeability in drug discovery and development settings. *Adv. Drug Delivery Rev.* **1997**, *23*, 3–25.

(25) Rodems, S. M.; Hamman, B. D.; Lin, C.; Zhao, J.; Shah, S.; Heidary, D.; Makings, L.; Stack, J. H.; Pollok, B. A. A FRET-based assay platform for ultra-high density drug screening of protein kinases and phosphatases. *Assay Drug Dev. Technol.* **2002**, *1*, 9–19.

(26) Leeson, P. D.; Springthorpe, B. The influence of drug-like concepts on decision-making in medicinal chemistry. *Nat. Rev. Drug Discovery* **2007**, *6*, 881–890.

(27) Please refer to Supporting Information for methodology.

(28) Rewcastle, G. W.; Palmer, B. D.; Thompson, A. M.; Bridges, A. J.; Cody, D. R.; Zhou, H.; Fry, D. W.; McMichael, A.; Denny, W. A. Tyrosine kinase inhibitors. 10. Isomeric 4-[(3-Bromophenyl)amino]-pyrido[*d*]-pyrimidines are potent ATP binding site inhibitors of the tyrosine kinase function of the epidermal growth factor receptor. *J. Med. Chem.* **1996**, *39*, 1823–1835.

(29) Fry, D.; Kraker, A.; Meyer, R. F.; Rewcastle, G. W. Bicyclic Compounds Capable of Inhibiting Tyrosine Kinases of the Epidermal Growth Factor Receptor Family. US Patent US5654307A1, 1997.

(30) Giannetti, A. M. From experimental design to validated hits a comprehensive walk-through of fragment lead identification using surface plasmon resonance. *Methods Enzymol.* **2011**, *493*, 169–218.

(31) Giannetti, A. M.; Koch, B. D.; Browner, M. F. Surface plasmon resonance based assay for the detection and characterization of promiscuous inhibitors. *J. Med. Chem.* **2008**, *51*, 574–580.